Neural Network Model for Tissue Thickness Estimation

Henna Jethani
Department of Electrical Engineering
University of Colorado at Boulder
Microwave Research Group

Zoya Popović
Department of Electrical Engineering
University of Colorado at Boulder
Microwave Research Group

***Abstract*—This paper explores the use of optimization methods to estimate thicknesses of subcutaneous tissues using a non-invasive near-field antenna with microwave low-power reflectometry from 2–13.5 GHz. The initial simple model assumes a planar tissue stack and is implemented with a Long Short-Term Memory (LSTM) neural network trained on full-wave electromagnetic simulation data. A stack of tissue phantoms for skin, fat and muscle with 2 and 3 layers is used for experimental validation. The application for the work presented in this paper is non-invasive internal body temperature measurement using microwave radiometry, where knowledge of tissue thicknesses and electrical parameters is required to solve the inverse problem. These parameters vary based on body composition and type, as well as the specific placement of the sensor on the body. For example, the outermost layer of the forearm epidermis varies by 4.9 mm and upper abdominal fat can vary by 15 mm between people. The model developed for this paper predicts thicknesses of a stackup of Playdough, Rogers Duroid 6010 and a commercial skin phantom within 7%, 42%, and 24% respectively, with a neural network loss value of 0.29. This preliminary model demonstrates the prediction of thicknesses of a more general N-layer stackup and serves as a proof of concept for a higher fidelity model that can be used to additionally predict dispersive permittivity and conductivity of layered tissues.**

***Index Terms*—Neural networks, RNN, LSTM, custom loss function, electromagnetics, tissue properties, core body temperature, radiometry, noninvasive, wearables.**

I. Introduction

As the size and computational demands of biological data has increased, the application of machine learning optimization methods to biological problems has proliferated in the last decade. In this paper we address the specific problem of *in-situ* measurement and estimation of sub-cutaneous tissue layer properties. The thicknesses, as well as other parameters such as permittivity, conductivity, mechanical and thermal properties of tissue layers are needed for design of e.g. antennas for body-area communication networks [1], wireless powering of implants [2], and wearable textile antennas [3]. All of these applications benefit from the understanding of tissue parameters as they directly affect the electromagnetic fields.

An application that is the motivation for the work in this paper is core body thermometry, illustrated in Fig. 1. There exists a demand for accurate, non-invasive core body temperature (CBT) monitoring. CBT differs from skin temperature, which undergoes fluctuations as a direct result of the environment. Typically, CBT is measured using invasive surgical probes, rectal or oesophageal sensors, which are generally expensive and are not solutions for continous, long-term monitoring [4]. Having the means to noninvasively and continuously capture fluctuations in core temperature can enable diagnostics of e.g. sleep disorders [5], and soldiers and athletes at the threshold of hyperthermia or heatstroke in extreme environments [6]. The current methods to noninvasively measure internal temperature are MRI [7] which is expensive and large, and heat-flux probes [8] which do not measure deep tissue temperature. A method to non-invasively determine sub-cutaneous temperature is microwave radiometry. Previous work in this field includes the

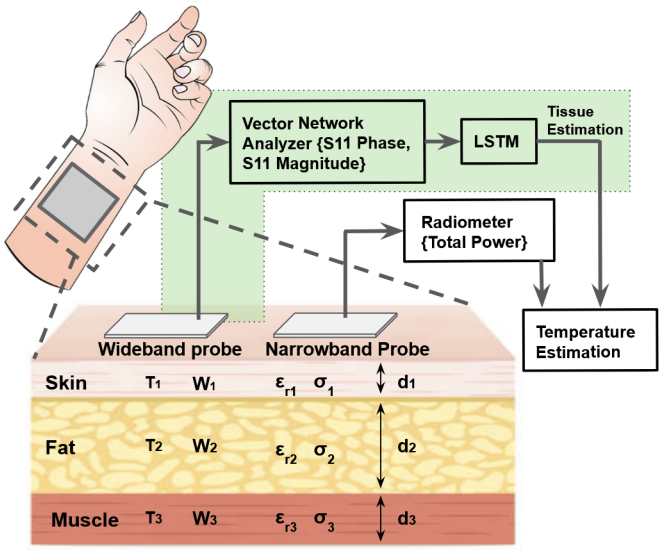

Fig. 1: Illustration of internal body thermometry setup with tissue estimation. The thermometer is a radiometer, in which a narrowband antenna and sensitive receiver measure total noise power proportional to temperature. Tissue-dependent weighting factors W_i are used to estimate individual layer temperatures T_i. To determine the layer properties $(d_i, \epsilon_{ri}, \sigma_i)$ a wideband antenna collects reflectometry data from a vector network analyzer (VNA) from 2 to 13.5 GHz, fed into a LSTM algorithm. The focus of this paper (indicated in green) is to determine the tissue layer thicknesses d_i.

This work was funded by the National Science Foundation, grant ECCS 2026523.

use of a 1.4 GHz near-field radiometer of a Dicke architecture for centimeter penetration of tissues for blackbody radiation retrieval in conjuction with tissue weighting functions that were obtained using full wave simulation [4], [9]. In [10], a radiometer for breast cancer detection in hospitals is shown. Lower frequencies need to be used for centimeter-sensing depth in tissues, e.g. the 27-MHz wide radioastronomy band at 1.4 GHz.

Fig. 1 shows the fundamental principle of a wearable radiometer integrated with a device that calibrates the tissue layers. The thermometer is a radiometer, in which a narrow-band antenna and sensitive receiver measure total noise power proportional to temperature. Tissue-dependent weighting factors W_i are used to estimate individual layer temperatures T_i. To determine the layer properties (d_i, relative permittivity ϵ_{ri} and conductivity σ_i) a wideband antenna collects reflectometry data from a vector network analyzer (VNA) from 2 to 13.5 GHz, which is then fed into a LSTM algorithm described in detail below. The focus of this paper is to determine the tissue layer thicknesses d_i.

This paper is organized as follows. Section II introduces the significance of the tissue thickness prediction and the methodology implemented to solve the problem. Section III provides a brief review of the effect that tissues parameters have on electromagnetic characteristics and the need for calibration. Next, Section IV reviews the configuration of the antenna in a full-wave electromagnetic simulator, describing how the training data is obtained. The neural-network architecture is described in Section V, while Section VI gives the performance results and experimental validation. Finally, some conclusions and avenues for future work are given.

II. Motivation and Approach

A narrow-band, near-field antenna placed on the skin receives the total noise power from all tissues under it, which is proportional to the bandwidth of the receiver, B, and the temperatures of all the layers under the antenna:

$$P = kB \sum_{i=1}^{N} W_i T_i \quad , \tag{1}$$

where k is the Boltzmann constant, and W_i, T_i are the weighting factor and temperature of the ith layer [4]. The weighting factors define the contributions that the tissue layers have to the overall power and are a direct function of tissue thickness d, frequency f, conductivity σ, and permittivity ϵ:

$$T = \sum_{i=1}^{N} W_i(f, d_1, \sigma_1, \epsilon_1 ... d_i, \sigma_i, \epsilon_i) T_i \quad . \tag{2}$$

The weight W_i of each layer is found from reciprocity as the power dissipated in a particular layer normalized to the total dissipated power when 1 W of power is incident from the antenna:

$$W_i = \frac{P_{di}(r)}{P_d} \quad , \tag{3}$$

where P_{di} is the power dissipated in the ith layer and P_d is the power dissipated in the entire volume. The size of the volume is bound by the power loss density values below 10 W/m^3, which captures more than 99% of the incident 1 W. This is determined in the full-wave electromagnetic solver by simulating the fields under the antenna [4].

In order to calculate the weighting factors, having a process for determining thickness, permittivity and conductivity is critical because they are required by the full-wave solver HFSS from Ansys [11]. These parameters are different across body compositions and body types, requiring "model calibration". Permittivity and conductivity are frequency-dependent while thickness is frequency-independent, and therefore we start the calibration using a neural network model to solve for tissue thickness of each layer in a 2-layer and 3-layer stackup, shown in Fig. 2. The training data from HFSS are first collected using a simulation of the complex reflection coefficient (S_{11}) of a broadband (2–13.5 GHz) near-field bow-tie antenna [12] against a stackup that is parameterized for varying layer thicknesses. The LSTM model is composed in Python using the Keras library [13]. The validation step occurs when the model is used to make a prediction on the reflection coefficient data collected from a VNA connected to the physical antenna placed on a comparable stackup.

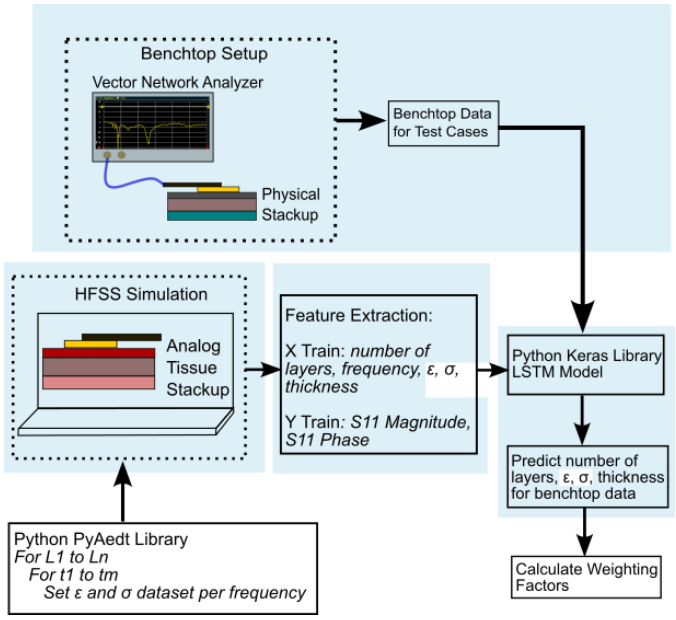

Fig. 2: Proposed workflow for applying a LSTM model to determine weighting factors. Areas highlighted in blue show the steps covered by the research presented in this paper. The reflection coefficient S_{11} amplitude and phase data from 2–13 GHz is acquired using a wideband antenna that is placed against a tissue stackup and the probe is connected to a VNA.

Tissue	Avg. Thickness [mm]	ϵ	$\sigma(S/m)$
Scalp	4	39.60	1.04
Skull (Cortical)	2.2	12.05	0.21
Skull (Cancellous)	1.8	19.90	0.47
Skull(Cortical)	1.4	12.05	0.21
Brain	50	47.30	1.50

TABLE I: (Region 1) Average thickness, permittivity and conductivity for each tissue layer at forehead [14], [15] and [16].

Tissue	Avg. Thickness [mm]	ϵ	$\sigma(S/m)$
Skin	1.2	39.60	1.04
Fat	4	11.15	0.15
Cortical Bone	2	12.05	0.21
Cancellous Bone	4	19.90	0.47
Cortical Bone	2	12.05	0.21
Heart	50	57.54	1.51

TABLE II: (Region 2) Average thickness, permittivity and conductivity for each tissue layer at the sternum [14], [15] and [16].

Tissue	Avg. Thickness [mm]	ϵ	$\sigma(S/m)$
Skin	2-4	39.66	1.04
Fat	10-30	5.4	0.07
Linea Alba	3	44.90	0.96
Muscle	9-11	54.11	1.14
Liver	10-21	45.12	1.08
Stomach	110	63.94	1.44
Pancreas	30-90	58.76	1.27

TABLE III: (Region 3) Average thickness, permittivity and conductivity for each tissue layer at the upper abdominal region of the body [17], [15] and [16].

Fig. 3: Top left shows a graphic representation of which body locations are described by their electromagnetic properties in Tables I, II, and III.

A. *Need for Calibration*

Factors including age, race, gender, and genetic history all affect the composition of muscle, fat, and tissue in the human body. In order for the internal thermometry tool to be effective across the general population, calibration for body composition should be accurately performed. Limited data exists in the literature on body composition across a diverse population. For example, [18] reports that although research groups have attempted to cover the variation in skin structure and function across diverse groups, these studies remain limited in their sample size or they focus on interindividual variations in skin quality and overlook racial differences. For skeletal muscle, which is the largest adipose tissue-free body mass in humans, [19] endeavors to close the gap by studying the differences across a racially diverse sample of 2000 people over an age range of 60 years.

A well-known experimental and theoretical study of electromagnetic tissue properties including conductivity and permittivity [20] includes variation across a broad frequency range in the microwave part of the spectrum, but does not include the diversity in the sample size. Other sources for electromagnetic tissue properties in the microwave range include [16] and full-body models are available from [21]. Although this data can be helpful, a practical application requires a fast measurement of tissue properties at a specific place where temperature data is acquired for a one-time calibration. In order to provide a non-invasive internal body thermometry tool that can be used inclusively across a population, the intent is to train the neural network across a wide range of thicknesses and frequency-dependent conductivities and permittivities to determine the weighting factors for different body compositions. The determination of tissue layer thicknesses described in this work is an important step toward bridging this gap.

III. Nature of Data

The data involved in the training for the calibration process of the noninvasive thermometer are the reflection coefficient, S_{11}, of the test antenna and thicknesses of the tissue layers under the antenna. The reflection coefficient, or scattering parameter, is defined as:

$$S_{11} = \frac{Z_L - Z_0}{Z_L + Z_0} \quad , \tag{4}$$

where Z_L is the effective impedance of the antenna on the tissue stack, and $Z_0 = 50\,\Omega$ is the characteristic impedance of the coaxial cable connected to the antenna. This parameter is complex because the lossy tissues are described with a

complex impedance. Therefore, both amplitude and phase need to be characterized. The thicknesses of the tissue layers impact the effective impedance seen by the antenna, and these vary across different regions of the body as well as between humans. Fig. 3 shows the electromagnetic properties across the sternum, forehead, and upper abdomen regions. This figure demonstrates the significant variability in tissue thickness across the body e.g. the difference in fat thickness between the sternum and the upper abdominal can be as much as 26 mm [14], [17].

IV. HFSS Model Setup

Training data is obtained from HFSS simulations of a near field wideband antenna against an analog tissue stackup. We use reciprocity and model the antenna as a transmitter with 1 W of transmitted power. An image of the antenna numerical model is shown in Fig. 4, and an example electric field vector magnitude distribution of the probe at 2.45 GHz is presented in Fig. 5. This demonstrates electric field penetration into all of the layers, where limitation exists in Playdough due to skin depth. The field distribution looks similar at all frequencies where the antenna is well matched.

The near-field antenna is simulated against two tissue stackups. The first stackup is composed of a commercial skin phantom manufactured by Speag [22], a low-loss microwave substrate (Rogers Duroid 6010) simulating fat, and Playdough simulating muscle. The second stackup is composed of the Speag skin phantom and Playdough. Frequency-dependent permitivity and conductivity are defined in the model for skin phantom and Playdough as they are dispersive. The permittivity and conductivity values over frequency are used from [12] and are shown in Fig. 6 and Fig. 7. The materials are modeled as impedance boundary layers in HFSS since they represent resistive layers that experience losses when fields and currents pass through the layers. Average permittivity, conductivity and thickness values of the materials used in this model are included in Table IV.

Simulations are executed for the two-layer and three-layer stackups over a range of thicknesses. The results include $|S_{11}|$ and $\angle S_{11}$ per iteration of thickness, per layer over the frequency range of 2–13.5 GHz. The training data set is composed of 447 permutations of layer thicknesses. The data is exported from HFSS to CSV files to be used as training data for the LSTM code.

A. Justification for Material Selection

In this preliminary phase of this research, it was necessary to utilize materials whose electromagnetic properties have been characterized in a lab environment and that are readily available to ensure reproducibility of results. Hence, the selection of Playdough and the Rogers Duroid 6010 substrate. Playdough is known in the bio-electromagnetic community to be a reasonable muscle phantom. The skin phantom was purchased from Speag. Fig. 8 shows a subset of the complex reflection coefficient curves that are used for the training data. The image shows significant variations when thicknesses

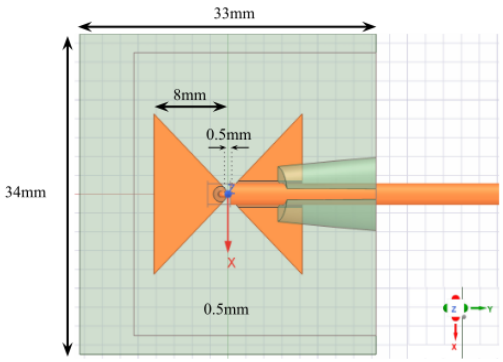

Fig. 4: Computational model of near-field, wideband probe model in HFSS.

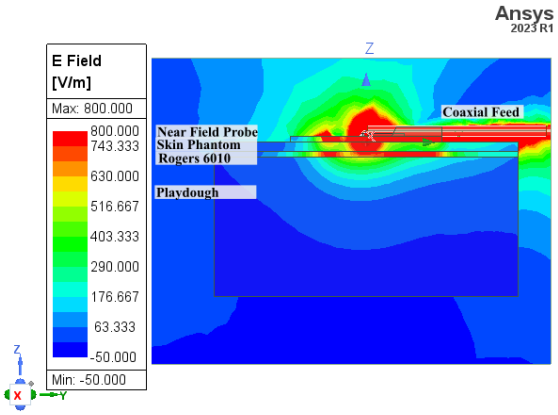

Fig. 5: Plot of magnitude of the electric field vector at 2.45 GHz for the broadband nier-field probe against a three layer stackup of 2.25 mm thick skin phantom, 1.91 mm thick Rogers 6010 substrate, and 30 mm thick Playdough.

of Rogers Duroid 6010 and skin phantom are iterated over, however insignificant changes when Playdough is updated since skin effect must be considered because Playdough is at 30 mm. Fig. 9 and Fig. 10 exhibit a comparison between an iteration of simulation data with the corresponding benchtop data, demonstrating that simulation data is a valid method for training the LSTM model.

TABLE IV: Stackup materials and corresponding average electromagnetic properties and thickness ranges for simulation.

Tissue	ϵ	$\sigma(S/m)$	**Thickness Range (mm)**
Skin Phantom (Speag)	24.3	1.98	1 to 3
Duroid (Rogers 6010)	10.2	-	1 to 3
Playdough	27	7	25 to 35

V. Neural Network Architecture

A. Neural Network Type Selection

Multi Level Perceptron (MLP) and Recurrent Neural Networks (RNN) were both considered when determining the architecture to apply to the internal thermometry calibration

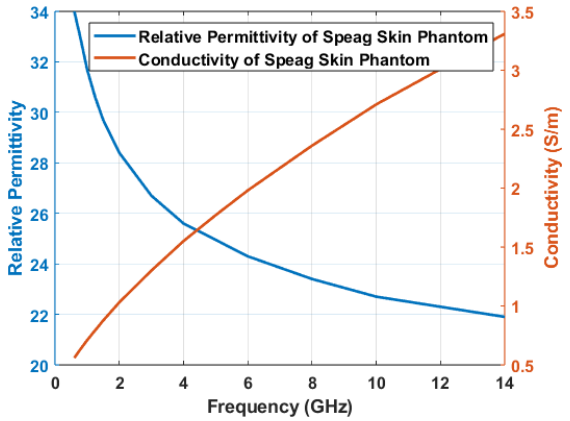

Fig. 6: Relative permittivity and conductivity over frequency for Speag skin phantom that are used in HFSS for simulation setup.

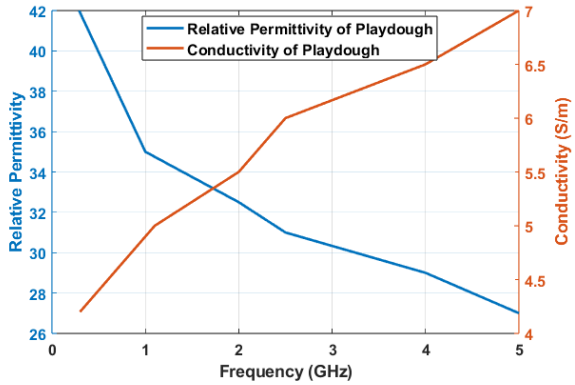

Fig. 7: Relative permittivity and conductivity over frequency for Playdough used in HFSS for simulation setup.

problem. Commonly, MLPs are applied to biomedical problems, however they are used when the predictions are based off static data. In the case of this project, the training data is frequency-dependent reflection coefficient and the predicted data for this preliminary step is number of layers and thickness of each layer in the tissue stackup. Future work involves additionally predicting frequency-dependent conductivity and permittivity of each tissue layer. Since the goal is to predict frequency-dependent data and the training data is over frequency, the neural network must capture sequential patterns to make predictions [23]. LSTMs are a specific type of RNN that are used to recognize long-term dependencies in temporal data [24].

B. Pre-processing Training Data

The input data is composed of three features: frequency, $|S_{11}|$ and $\angle S_{11}$. Thickness is changed for each layer in the stackup and for each thickness, the resulting $\angle S_{11}$ and $|S_{11}|$ are measured over the 2 GHz to 13.5 GHz frequency range by the solver. The data needs to be restructured and scaled appropriately prior to using it in the LSTM model. The X training data set is composed of frequency, $|S_{11}|$, and $\angle S_{11}$. The Y data is composed of the number of layers and their thicknesses. A graphic representation of the X and Y dataset

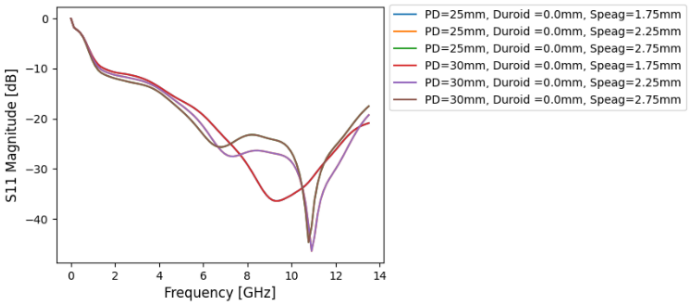

(a)

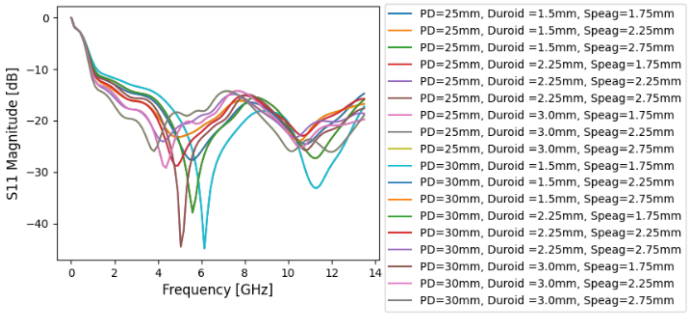

(b)

Fig. 8: (a) A subset of the simulation results from HFSS for a 2 layer stackup. The curves demonstrate that varying the Playdough thickness does not cause variation in the S_{11} curves, unlike variation in the skin phantom. This effect is due to skin depth. (b) A subset of the simulation results from HFSS for a 3 layer stackup.

division is presented in Fig. 11. Each feature is scaled by the minimum and maximum values of that feature. In the model, 70 % of the data is used for training and 30 % is used for test. The sequences of data were randomly shuffled when training and testing datasets were configured.

C. Neural Network Design

The initial layer of the model consists of 50 units accompanied with the 'Tanh' activitation function, which offers larger gradients around its zero center, which can capture minor changes in the sequential data. Tanh was chosen over Rectified Linear Unit (ReLU) to avoid the "dying ReLU" problem, when ReLU neurons become inactive and output zero in turn no longer contributing to the model learning process [25]. This must be avoided in order for intricacies of the temporal data to be detected by the LSTM.

Dense layers follow the initial layer, concluding with the final dense layer consisting of four units, addressing the four output parameters: number of layers, Playdough thickness, Rogers 6010 thickness, and Speag skin phantom thickness. Dropout layers were additionally incorporated for regularization and to prevent overfitting [26] and [27]. The architecture of the data flow for both the LSTM model and the experimental data validation process is shown in Fig. 12.

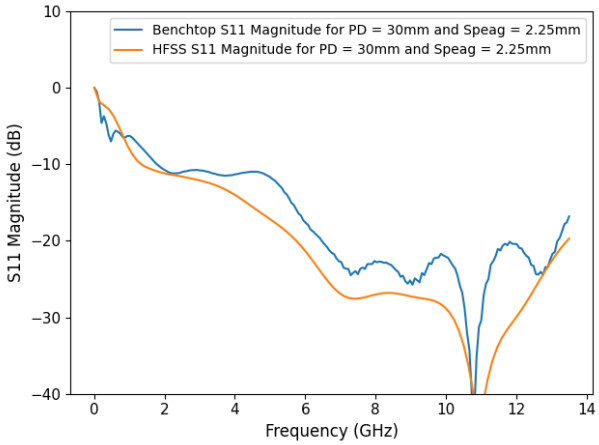

(a)

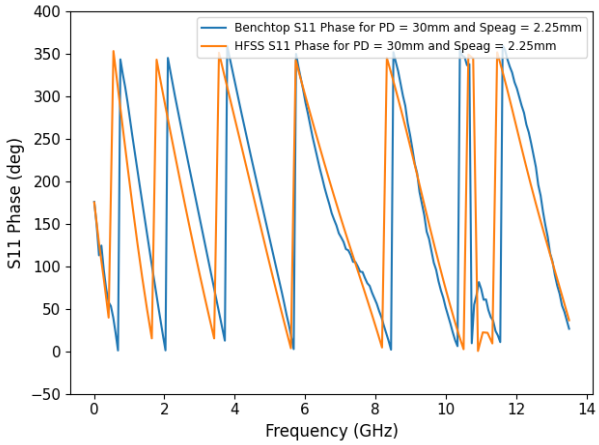

(b)

Fig. 9: (a) Experimental reflection coefficient magnitude plotted against simulated reflection coefficient magnitude over frequency for a two-layer stackup composed of Playdough and commercial tissue phantom, Speag. (b) Experimental reflection coefficient phase plotted against simulated reflection coefficient phase over frequency for a two-layer stackup composed of Playdough and commercial tissue phantom, Speag.

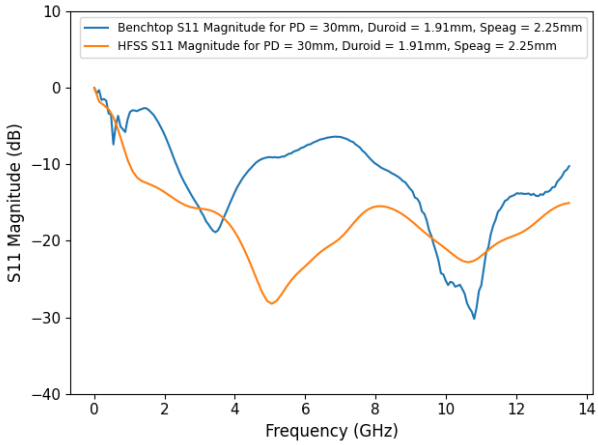

(a)

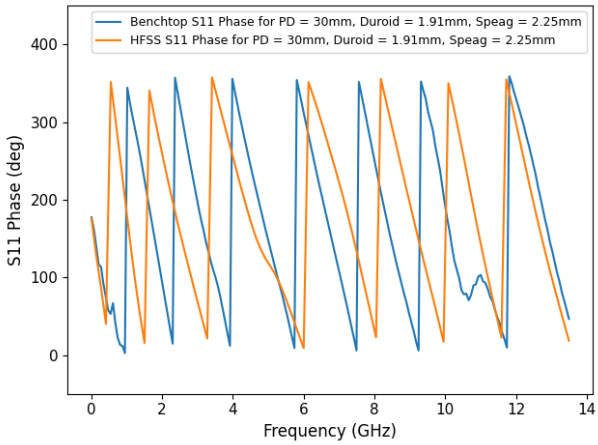

(b)

Fig. 10: (a) Measured and simulated reflection coefficient magnitude (a) and phase (b) for a three-layer stackup composed of Playdough, Rogers Duroid 6010, and commercial skin phantom from Speag. (b) Experimental reflection coefficient phase plotted against simulated reflection coefficient phase over frequency for a three-layer stackup composed of Playdough, Rogers 6010 Duroid, and commercial tissue phantom, Speag.

D. Custom Loss Function

A custom loss function is devised to address the physical constraints of the problem as well as minimize prediction errors [28]. The loss function incorporates the requirements that the number of layers prediction must be an integer and that thickness values are non-negative and within a reasonable band corresponding to the material nature of that layer. For example, the Speag skin phantom prediction is constrained to be on an order of a millimeter, but can be further constrained.

The loss function is composed of a mean squared error (MSE) term with penalty terms for conditions including non-integer values for number of layers and negative values for layer thicknesses [29]. The penalty for non-integer values is determined by calculating the absolute difference between the number of predicted layers and the closest integer value. Then penalties are calculated for negative thicknesses, which cannot physically exist. The penalties are further combined with coefficients that are used as weights to prioritize different facets of the problem. Combining all the coefficients with the penalties provided a total loss function that is used by the model to modify weights during training.

In the case that the experimental data is not over the complete frequency range covered in the training data, a linear interpolation with extrapolation for data outside the given frequency range is incorporated in the model.

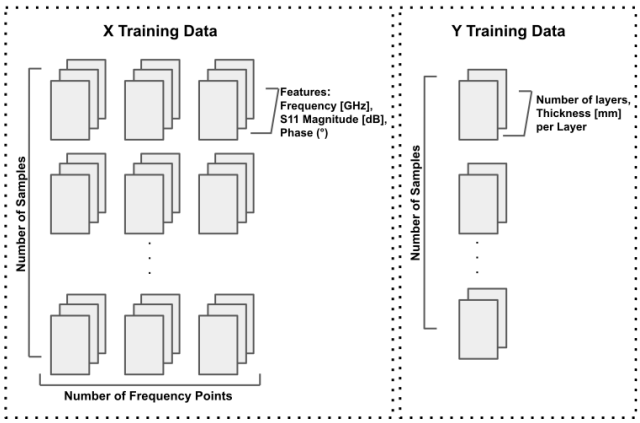

Fig. 11: Graphic representation of training and test data.

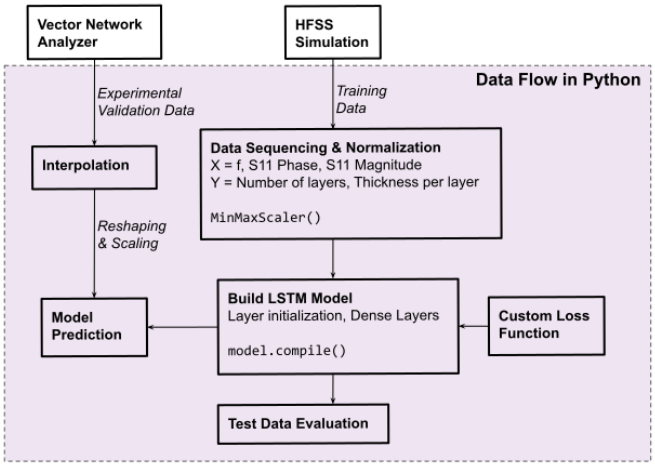

Fig. 12: Illustration of data flow and LSTM model build in Python.

VI. Performance Results and Experimental Validation

When evaluating the performance of the model, a few metrics are observed including the loss obtained as well as the predictions that the model made for benchtop measurements.

Fig. 13 shows the learning curve for both training and validation loss, as defined in [30] and [31]. Validation split of 0.3 is used, therefore 30% of the training data is used for validation. This curve shows how the performance of the model improves over the number of epochs. Over a training process of 200 epochs, the final training loss is 0.25, the final validation loss is 0.31 and the model test loss is 0.29. These loss values indicate that the model is performing at an adequate standard, however there remain opportunities for improvement, e.g. using more training data.

In addition to evaluating the performance of the model from simulation data for training and testing, it was imperative to use the model to make predictions on physical data obtained from a benchtop setup. A 10 MHz to 13.5 GHz VNA was used with the near field bow tie antenna that has been modeled in HFSS against a stackup of Playdough, Rogers 6010 and Speag

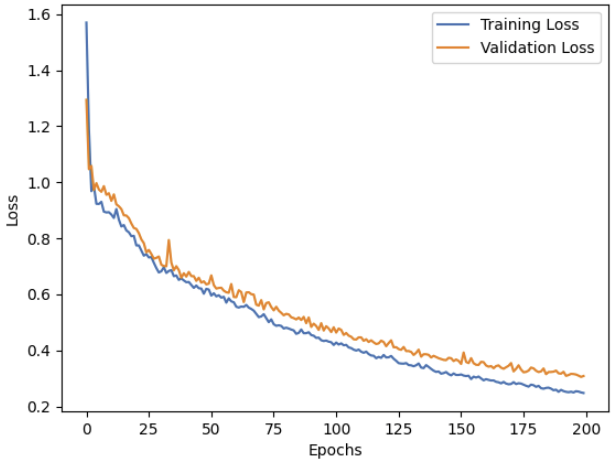

Fig. 13: Learning curve of the training and validation losses over epochs. This graph demonstrates that the model is neither underfitting nor overfitting the data since the validation and training loss curves follow one another closely and their respective values decrease over the training period.

skin phantom. Two physical stackup setups are used for this preliminary verification phase. The first is a two-layer model composed of the skin phantom and Playdough and the second uses all three materials. The resulting $|S_{11}|$ and $\angle S_{11}$ values from the VNA are used to make predictions on the thickness of each layer as well as the number of layers. The comparison between the benchtop values and the values predicted by the neural network model are shown in Table V.

TABLE V: Actual parameters of the experimental setup compared to the LSTM predictions of the experimental setup.

Test Type	Predicted No. of Layers	Layer Type	True Thickness [mm]	Predicted Thickness [mm]
2 Layer	2.32	Playdough Rogers 6010 Speag	30 0 2.25	28.10 0.56 1.71
3 Layer	2.75	Playdough Rogers 6010 Speag	30 1.91 2.25	29.783 1.109 1.86

Variation between the true values and predicted values are likely a result from the deviation between the benchtop S11 curves compared to those outputted from HFSS as shown in Fig. 9 and Fig. 10. This could be from a number of factors such as the materials are not exact to their datasheets, the Playdough experienced drying from when it was fitted etc.

VII. Conclusions and Discussion

In summary, this paper presents the use of an LSTM model trained on full-wave electromagnetic simulation data to estimate thicknesses of subcutaneous tissues using a non-invasive near-field antenna with microwave low-power reflectometry from 2–13.5 GHz. The application for the work presented in this paper is non-invasive internal body temperature measurement using microwave radiometry, where knowledge of tissue

thicknesses and electrical parameters are required to solve the inverse problem. These parameters vary based on body composition and type, as well as the specific placement of the sensor on the body.

This research shows that thickness for 2 and 3-layer experimental stackups of Playdough, Rogers Duroid 6010, and commercial skin phantom can be predicted within 7%, 42%, and 24% respectively, using the LSTM model described in this paper. This tolerance is satisfactory for the limited stackup presented here, however in the next phase of this study, this model will be extended to N = 4, 5, and 6 layers. Having established a method for predicting tissue thickness, the next phase of the research will extend the model to predict permittivity and conductivity across frequency and with variance among people. The high-level methodology for incorporating these parameters is shown in Fig. 1. The HFSS PyAedt API will be utilized to connect with HFSS to efficiently update conductivity and permittivity per frequency point. This must be done utilizing the API since these frequency-dependent parameters cannot be parameterized in HFSS itself. To reduce computational overhead, the permittivity and conductivity will be fitted to the Cole-Cole model, which will reduce complexity and eliminate the need for arbitrary values per frequency point [32].

Future work will incorporate validation with finite-difference time-domain electromagnetic simulations that will be performed using the Sim4Life tool [21]. Additionally, materials with well documented properties, including various tissue phantoms as well as animal models, can be used to improve the training data.

VIII. Acknowledgements

The authors would like to express their gratitude to Dr. Robert Streeter for providing the near-field wideband 2-20 GHz antenna and its simulation file for the collection of the experimental data and the simulations for the initial training data benchmark. The authors thank PhD student, Sofia Mvokany, at the Microwave Research Group at CU Boulder, for providing the characterization of Playdough that was used in the simulation file. The authors acknowledge funding from the National Science Foundation, grant ECCS 2026523.

References

[1] S. Movassaghi, M. Abolhasan, J. Lipman, D. Smith, and A. Jamalipour, "Wireless body area networks: A survey," *IEEE Communications surveys & tutorials*, vol. 16, no. 3, pp. 1658–1686, 2014.

[2] H. J. S. Kim Sanghoek and P. A. SY, "Wireless power transfer to miniature implants: Transmitter optimization," *IEEE Transactions on Antennas and Propagation*, vol. 60, no. 10, pp. 4838–4845, 2012.

[3] P. Salonen, Y. Rahmat-Samii, and M. Kivikoski, "Wearable antennas in the vicinity of human body," in *IEEE Antennas and Propagation Society Symposium, 2004.*, vol. 1, pp. 467–470 Vol.1, 2004.

[4] P. Momenroodaki, W. Haines, M. Fromandi, and Z. Popovic, "Non-invasive internal body temperature tracking with near-field microwave radiometry," *IEEE Transactions on Microwave Theory and Techniques*, vol. 66, no. 5, pp. 2535–2545, 2018.

[5] M. Uchiyama, M. Okawa, K. Shibui, K. Kim, H. Tagaya, Y. Kudo, Y. Kamei, T. Hayakawa, J. Urata, and K. Takahashi, "Altered phase relation between sleep timing and core body temperature rhythm in delayed sleep phase syndrome and non-24-hour sleep–wake syndrome in humans," *Neuroscience Letters*, vol. 294, no. 2, pp. 101–104, 2000.

[6] M. T. Veltmeijer, T. M. Eijsvogels, D. H. Thijssen, and M. T. Hopman, "Incidence and predictors of exertional hyperthermia after a 15-km road race in cool environmental conditions," *Journal of Science and Medicine in Sport*, vol. 18, no. 3, pp. 333–337, 2015.

[7] E. J. W. W. G. Galiana, R.T. Branca, "Accurate temerature imaging based on intermolecular coherence in magnetic resonance," *Science*, vol. 322, no. 5900, 2008.

[8] 3M, "Temperature monitoring." https://www.3m.co.uk/3M/enGB/Medical-GB/products/patient-monitoring/temperature-monitoring/. Accessed on October 14, 2023.

[9] J. Lee, G. S. Botello, R. Streeter, K. Hall, and Z. Popović, "A hybrid correlation-dicke radiometer for internal body thermometry," in *2022 52nd European Microwave Conference (EuMC)*, pp. 464–467, 2022.

[10] RES.LTD, "Microwave radiometry in mammology." http://resltd.ru/eng/radiometry/mom.php, 2023. Accessed on October 5, 2023.

[11] "Ansys." https://www.ansys.com/.

[12] R. Streeter, *High-resolution Deep-tissue Microwave Thermometry*. PhD thesis, University of Colorado at Boulder, 2023.

[13] Keras-team, "keras." https://github.com/keras-team/keras. Accessed July 2023.

[14] P. Momenroodaki, *Radiometric Thermometry for Wearable Deep Tissue Monitoring*. PhD thesis, Univeristy of Colorado at Boulder, 2017.

[15] ItalianNationalResearchCouncil, "Dielectric properties of body tissues." http://niremf.ifac.cnr.it/docs/DIELECTRIC/Title.html, 2023.

[16] ITISFoundation, "Dielectric properties." https://itis.swiss/virtual-population/tissue-properties/database/dielectric-properties/, 2023. Accessed on September 5, 2023.

[17] K. F. Torgutalp ŞŞ, "Abdominal subcutaneous fat thickness measured by ultrasound as a predictor of total fat mass in young and middle aged adults," *Acta Endocrinol (Buchar)*, vol. 18, pp. 58–63, 2022.

[18] A. V. Rawlings, "Ethnic skin types: are there differences in skin structure and function?1," *International Journal of Cosmetic Science*, vol. 28, no. 2, pp. 79–93, 2006.

[19] A. M. Silva, W. Shen, M. Heo, D. Gallagher, Z. Wang, L. B. Sardinha, and S. B. Heymsfield, "Ethnicity-related skeletal muscle differences across the lifespan," *American Journal of Human Biology*, vol. 22, no. 1, pp. 76–82, 2010.

[20] S. Gabriel, R. W. Lau, and C. Gabriel, "The dielectric properties of biological tissues: Iii. parametric models for the dielectric spectrum of tissues.," *Physics in Medicine and Biology*, vol. 41, no. 11, 1996.

[21] Z. M. Tech, "Sim4life academic." Accessed on October 14, 2023.

[22] SchmidPartnerEngineeringAG, "Swiss speag." https://speag.swiss/. Accessed on October 7, 2023.

[23] S. Hochreiter and J. Schmidhuber, "Long short-term memory," *Neural computation*, vol. 9, pp. 1735–80, 12 1997.

[24] B. Lindemann, T. Müller, H. Vietz, N. Jazdi, and M. Weyrich, "A survey on long short-term memory networks for time series prediction," *Procedia CIRP*, vol. 99, pp. 650–655, 2021. 14th CIRP Conference on Intelligent Computation in Manufacturing Engineering, 15-17 July 2020.

[25] L. Lu, Y. Shin, Y. Su, and G. Karniadakis, "Dying relu and initialization: Theory and numerical examples," 03 2019.

[26] SaturnCloud, "How to implement dropout in lstm neural networks with tensorflow." https://saturncloud.io/blog/how-to-implement-dropout-in-lstm-neural-networks-with-tensorflow/: :text=Dropout

[27] A. G, "A review of dropout as applied to rnns." https://adriangcoder.medium.com/a-review-of-dropout-as-applied-to-rnns-72e79ecd5b7b, 2018.

[28] S. Cloud. https://saturncloud.io/blog/custom-loss-function-for-rnn-lstm-in-keras-a-comprehensive-guide/custom-loss-function-for-rnn-lstm-in-keras-a-guide, 2023. Accessed on September 2, 2023.

[29] E. J. Skinner. https://towardsdatascience.com/creating-a-innovative-custom-loss-function-in-python-using-tensorflow-and-fitting-a-lstm-model-ded222efbc89, 2023.

[30] R. Pramoditha, "Plotting the learning curve to analyze the training performance of a neural network." https://medium.com/data-science-365/plotting-the-learning-curve-to-analyze-the-training-performance-of-a-neural-network-4a35818d01f2.

[31] C. Perlich, *Learning Curves in Machine Learning*, pp. 577–580. Boston, MA: Springer US, 2010.

[32] S. Gabriel, "Modelling the frequency dependence of the dielectric properties to a 4 dispersions spectrum.." http://niremf.ifac.cnr.it/docs/DIELECTRIC/AppendixC.htmlC01, 2023.